Stress profile of infant rib in the setting of child abuse: A finite element parametric study

Andy Tsai [a,*], Brittany Coats [b], Paul K. Kleinman [a]

[a] Department of Radiology, Children's Hospital Boston, Harvard Medical School, 300 Longwood Avenue, Boston, MA 02115, United States
[b] Department of Mechanical Engineering, University of Utah, Salt Lake City, UT, United States

ABSTRACT

The primary goal of this study is to advance our current understanding of infant rib injuries in the setting of child abuse. To this end, we employed finite element model simulations to determine the sensitivity of an infant rib's stress response to varying material properties and under varying degrees of anterior–posterior chest compression. Using high-resolution chest CT images obtained from a 6-day-old infant, we constructed a simplified geometric model consisting of bone and cartilage structures. To simulate the lateral gripping of an infant in child abuse, an anterior–posterior chest compression load was applied to cause increased stresses along the costovertebral articulation, a classic site for inflicted rib fractures. A sensitivity analysis was conducted to quantify the effects of varying Young's modulus and Poisson's ratio of the bones and cartilages. In addition, we varied the amount of anterior–posterior chest displacement to assess the sensitivity of this parameter to the rib's stress profile. We found that varying Young's modulus of the bone and cartilage not only changed the magnitude but also the shape profile of the rib's stress response. In contrast, varying the degree of chest compression only changed the magnitude of the stress response and *not* the shape profile. We also discovered that by varying Poisson's ratio of the bone and cartilage, no appreciable change was seen in the magnitude or the shape profile of the rib's stress response. Finite element modeling shows promise as a tool to elucidate the mechanisms of rib fractures in abused infants.

© 2012 Elsevier Ltd. All rights reserved.

1. Introduction

Unlike adults, in whom rib fractures are frequent and often caused by direct impact, rib fractures in infancy (≤ 12 months old) are uncommon and often caused by child abuse (Worn and Jones, 2007). Although direct impact may occasionally play a role, manual thoracic compression is generally assumed to be the cause of most inflicted infant rib fractures (Betz and Liebhardt, 1994; Kleinman, 1990; Kleinman et al., 1996; Kleinman and Schlesinger, 1997; Reece, 1993, 2002, Worn and Jones, 2007). Fractures near the costovertebral articulations are highly associated with infant abuse, and although anterior–posterior compression of the rib cage during assaults is supported by perpetrator confessions and injury morphology, rigorous laboratory research that characterizes the type and magnitude of force required to cause inflicted rib fractures is lacking (Boal, 2008; Kleinman, 1990; Lonergan et al., 2003; Reece, 1993). Attempts to understand infant rib fracture with *in vivo* experimentation are not feasible. Finite element (FE) modeling offers an attractive alternative to develop a scientific foundation

for investigating these theories. Thus, the goal of this paper is to begin the development of an FE model that can be used to advance our current understanding of infant rib fractures and better understand the biomechanical response of infant ribs during child abuse.

While there are numerous reports of the biomechanical response of adult ribs under stress using the FE modeling (Charpail et al., 2005; Ito et al., 2009; Kemper et al., 2005; Li et al., 2010a, 2010b; Niu et al., 2007; Ruan et al., 2003; Yoganandan and Pintar, 1998), similar information on infant ribs is lacking, mostly because there is very little material property data on infant ribs. To our knowledge, there is only one study that reported the material properties of pediatric ribs (Pfefferle et al., 2007). In that study, Young's modulus, yield force, and rib stiffness of the pediatric rib bone were explored in 13 subjects ranging in age from 1-day-old to 72-months-old. As is typical in studies with limited human specimen availability, variability is large and identifying representative properties for the FE modeling is challenging. Therefore, the objective of this study was to identify the material properties that most influence the infant rib stress response during abusive chest compression, and ascertain whether changes in chest compression depth significantly alter patterns of stress. These findings will provide preliminary data that can direct future research for predicting rib fracture in children.

* Corresponding author. Tel.: +1 857 218 5102; fax: +1 617 730 0635.
 E-mail address: andy.tsai@childrens.harvard.edu (A. Tsai).
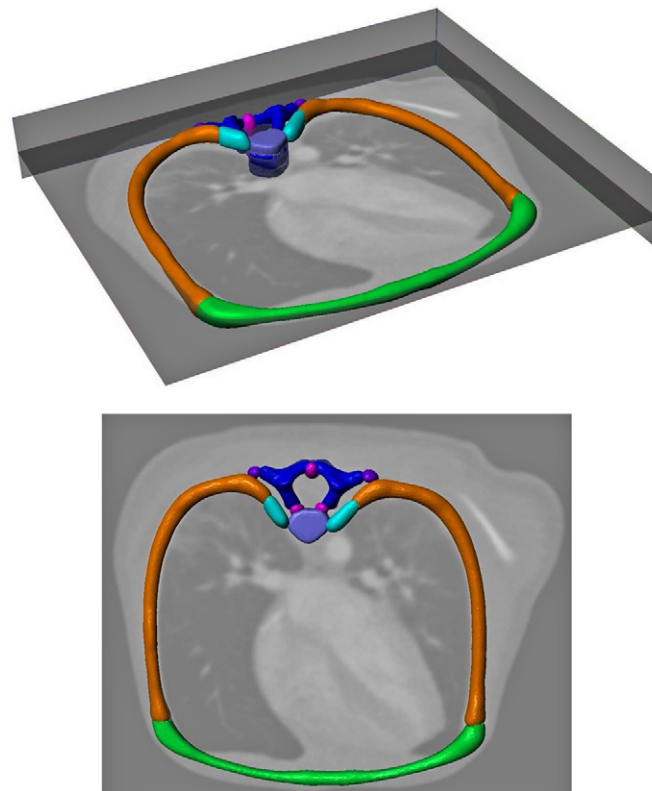
2. Methods

2.1. Geometry

For anatomic fidelity of an infant's chest, the geometry of the FE rib model was constructed based on a chest CT of a 6-day-old boy (approved by the Institutional Review Board at Children's Hospital Boston), with 0.28×0.28 mm in-plane resolution, 2 mm slice thickness, 80 KVp, 90 mAs, and pitch of 1. This chest CT, acquired on a Siemens Sensation 64 multi-detector CT (Siemens Medical Solutions, Malvern, PA), was initially performed to investigate a small lucent lung lesion found on a chest radiograph taken in the setting of respiratory distress. This lucent lesion was found to represent a small loculated pneumothorax that resolved on a follow up study.

The FE model was focused on a single rib pair, as a high-resolution model consisting of the entire rib cage and associated soft tissue would be computationally intractable. The FE geometry was derived by using a semiautomated segmentation algorithm, which included a combination of intensity thresholding (> 120/255), 3D region growing, morphologic filtering, and 3D Gaussian smoothing to outline the smooth bony contour of the sixth rib and vertebral body (ScanIP, Simpleware Ltd., Exeter, UK). The sixth rib was selected because this is a "true" rib and most rib fractures in abused infants occur in the mid portion of the rib cage (Kleinman et al., 2000). The rib bone was modeled as a homogeneous solid structure without separating it into cortical and trabecular components due to the poor spatial resolution of CT in differentiating these components (Fig. 1). The sixth rib pair in infants is relatively horizontal and planar in configuration compared to adult rib pairs (Openshaw et al., 1984). The contours of the cartilage structures (inter-vertebral disks, anterior costal cartilage, rib head and transverse process cartilage apophyses, and vertebral synchondroses cartilage) could not be identified on CT; hence, these structures were created based on anatomical atlases (Gray, 1974; Netter, 2003). The sternum at the level of the sixth rib is cartilaginous and has not yet ossified at this age.

The final $442 \times 363 \times 64$ voxel model had an isotropic voxel resolution of 0.28 mm (Fig. 2). The sixth rib was approximately 8.4 cm long. The anterior–posterior diameter of the thorax was 9.2 cm. The circumference of the thorax, including the overlying soft tissue, was 33.5 cm. The model had a slight right–left asymmetry that is within the range of normal anatomic variability.

2.2. Material properties

For simplicity, bone and cartilage were modeled as isotropic elastic materials using Navier–Cauchy equations. As such, Poisson's ratio and Young's modulus E were necessary components for the FE simulations. A FE parametric study was performed to determine the influence of Young's modulus and Poisson's ratio of

Fig. 1. Chest CT and 3D rendering of a 6-day-old infant's bony thorax. The axial and coronal CT images along the left column illustrate the bone density along the axial and coronal planes of the infant's 6th rib. Notice the poor spatial differentiation between the bone's cortex and trabecula due to its diminutive size. The right column demonstrates two 3D renderings of the bony thorax based on the chest CT. The paired sixth rib is outlined in orange, while the sixth vertebral body is outlined in blue. Notice the relatively planar and horizontal configuration of the rib pairs, with the sixth rib pair oriented nearly perpendicular to the axis of the spine. (For interpretation of the references to color in this figure legend, the reader is referred to the web version of this article.)

Fig. 2. Two views of the single rib pair model. In keeping with anatomic imaging, the right rib is to the left of the image while the left rib is to the right of the image. The anatomic structures include paired sixth rib (orange), sixth vertebral body (dark blue), inter-vertebral disks (light purple), rib head cartilage apophyses (cyan), transverse process cartilage apophyses (dark purple), vertebral synchondroses cartilage (magenta), and anterior costal cartilage (green). (For interpretation of the references to color in this figure legend, the reader is referred to the web version of this article.)

bone and cartilage on stress magnitude and distribution during infant chest compression. We chose to evaluate von Mises stress σ_{vm} for analysis.

2.2.1. Bone

The same material properties were assigned to the rib and vertebral body. A low, baseline, and high value were used for each of the properties.

Young's modulus. The baseline value was chosen based on the following non-linear relationship between Young's modulus of cortical bone and biological age developed by Pfefferle et al. (2007):
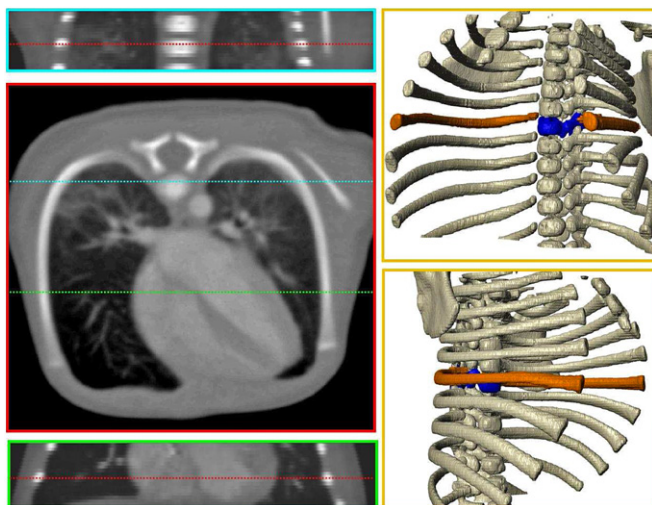
$$E = 138.99x^{0.7996} \tag{1}$$

where x is the age in months. Using this equation, we estimated the baseline modulus of a 6-day-old infant to be 38 MPa. Because there was a significant amount of variability in the pediatric rib measurements, the low value for the modulus (9 MPa) was obtained by plugging the biological age of 1-day (the youngest specimen in that study) into Eq. (1). The high value for the modulus (9 GPa) was the largest data point provided in Pfefferle's study.

Poisson's ratio. The baseline value for Poisson's ratio was set at 0.379, which is the average value from adult rib bone (Abe et al., 1996; Greer, 2006; Viano, 1986). The low value for Poisson's ratio (0.3) was Poisson's ratio of the adult cortical bone (Li et al., 2010a, 2010b). By purposely choosing Poisson's ratio of the cortical bone (which is harder and denser than trabecular bone), we positioned ourselves at the low end of the scale for this parameter. Using a similar argument, the high value for Poisson's ratio (0.45) was Poisson's ratio of the adult trabecular bone (Li et al., 2010a, 2010b).

2.2.2. Cartilage

The same properties were assigned to all the cartilage structures. A low, baseline, and high value were used for each of the properties.

Young's modulus. The baseline value for Young's modulus (2.3 MPa) is the modulus reported for a 3-year-old child's cartilage (Mizuno et al., 2005). While this measurement reflects that of a toddler, it remains the nearest approximation in age (found in the literature) to the 6-day-old infant selected for our study. The low value for the modulus (0.06 MPa) is representative of the cartilage anlagen of

a fetal talus (Mahmoodian et al., 2009). The high value for the modulus (49 MPa) is the highest value given in the adult literature surveyed (Forman et al., 2010; Forman and Kent, 2011; Lau et al., 2008; Yamada, 1970).

Poisson's ratio. The baseline value of Poisson's ratio (0.4) is the most commonly used value for cartilage in adult FE models (Greer, 2006; Mahmoodian et al., 2009; Vaziri et al., 2009; Yamada, 1970). The low value (0.36) is the lowest Poisson's ratio found in the literature (Trickey et al., 2006). The high value (0.49) is the highest Poisson ratio found in the literature (Forman and Kent, 2011).

2.3. Mesh development

The mesh was created in ScanIP using 4-node tetrahedral elements. Nodes from different materials were tied to one another along their boundaries. Static analysis simulations were completed using COMSOL (COMSOL, Inc., Burlington, MA) on an HP Z600 workstation with dual Intel 2.4 GHz Xeon Quad-Core processor (Hewlett-Packard Co., Palo Alto, CA). A convergence study was performed (Section 3.1) to evaluate the stability and mesh independence of the FE model prior to conducting the sensitivity study.

2.4. Boundary conditions

To our knowledge, there are no published reports describing how much force is needed to fracture infant ribs in the setting of abuse. Hence, instead of specifying an applied force, displacements were prescribed as an indirect mechanism of generating compressive force. These displacements were varied to identify changes in stress distribution with compression depth. The point of reference for a reasonable amount of infant chest displacement was the American Heart Association (AHA) recommendations for infant CPR. Specifically, chest compression depth should be one-third of the anterior–posterior dimension of the chest (AHA, 2006). The anterior–posterior dimension of the infant thorax was approximately 9.2 cm, so one-third (3.06 cm) was selected to represent the baseline anterior–posterior chest displacement. The low and high values for the amount of chest displacement were set at one-fourth and one-half of the anterior–posterior chest dimensions, respectively.

It is widely believed that during abuse, the infant is held facing the assailant with palms along the infant's side, the long fingers positioned posteriorly along the spine, and the thumbs positioned slightly apart over the anterior chest wall (Kleinman, 1990; Lonergan et al., 2003; Reece, 1993, Slovis, 2008). The average single hand span of an adult male and female is 22.6 cm and 20.6 cm, respectively (Wagner, 1988). The average hand length of an adult male and female is 19.3 cm and 17.9 cm, respectively (Donelson and Gordon, 1996). Hence, an average adult, with two hands held together, can completely encircle the thorax of this infant. The forceful lateral gripping of the hands with the fingers positioned as depicted in Fig. 3 would simulate squeezing of the chest in the anterior–posterior plane, as in the setting of child abuse. Fingers were positioned as such to generate increased stress near the costovertebral articulation, a classic location for inflicted rib injuries, but unusual for rib fractures of other causes in infancy (Kleinman et al., 1996). The surface contact points (denoted by yellow and red bars in Fig. 3) correspond to the contact footprints of the assailant's finger tips. The width of the posterior contact points was set empirically at 3.2 cm, the approximate length of two distal phalanges combined. The width of each of the two anterior contacts was set empirically at 1.6 cm, the approximate length of the distal phalanges of
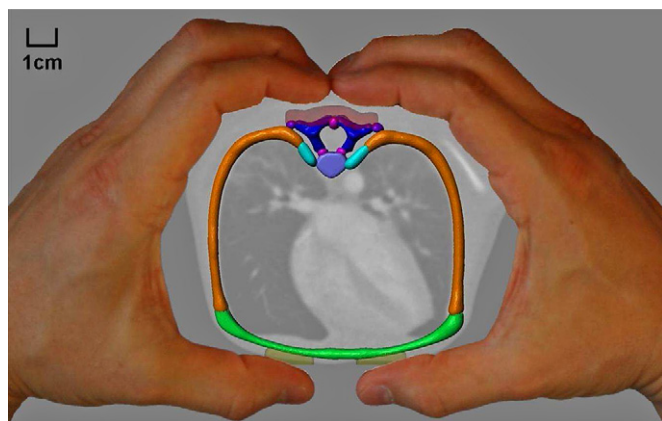
the thumb. The anterior surface displacement footprints were empirically positioned 1.4 cm apart.

2.5. Data collection and analysis

Baseline computer simulations were performed first, followed by independent variation of each material property, yielding a total of 11 simulations. For each simulation, the longitudinal axis of each rib was partitioned into 10 cylindrical segments of equal size (Fig. 4). Segment 1 corresponds to the anterior sternal end of the rib; Segments 2–7 correspond to the rib body; Segments 8 and 9 correspond to the posterior rib arc; and Segment 10 corresponds to the rib head, neck, and tubercle. The average stress and standard deviation was calculated within each of these segments for analysis.

3. Results

3.1. Mesh convergence study

The average element edge length was varied from 0.416 mm (employing 831,812 elements) to 1.438 mm (employing 49,222 elements). A total of 11 simulations, each using a different mesh size, were performed. The percent difference in the average stress within each rib segment (relative to the densest mesh model) was then plotted as a function of mesh size (Fig. 5). Specifically, Δ_i^m, the percent difference in stress in rib segment i using average element edge length m, was defined as
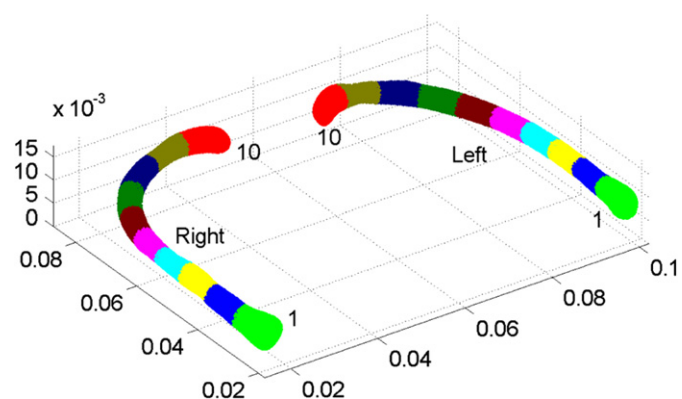
$$\Delta_i^m = \frac{\sigma_{vm_i}^m - \sigma_{vm_i}^M}{\sigma_{vm_i}^M} \times 100, \tag{2}$$

where $\sigma_{vm_i}^m$ denotes the average stress within rib segment i while using an average element edge length m. The densest mesh used in this analysis had an edge length of $M=0.416$ mm. Above $m=1.065$ mm, there was an overall sharp increase in Δ_i^m. We selected $m=1.065$ mm as the optimal mesh size (84,232 elements) because they were only $<7\%$ different from the densest mesh simulations, and resulted in a solution time that was <18 min. This small error is likely due to variability while sorting the very large number of elements from each mesh into small rib segments.

3.2. Parametric study

3.2.1. Baseline simulation

The simulation results of the single rib pair model, using baseline values for the material properties and chest compression depth, show an open-book type of anterior rib motion, with compressive lateral bowing in the anterolateral aspects of both

Fig. 3. Hand-positioning during lateral grabbing of an infant, depicted to scale. Positions of the anterior displacement points are depicted by the two faint yellow bars. Positions of the posterior displacement points are depicted by the faint red bar. (For interpretation of the references to color in this figure legend, the reader is referred to the web version of this article.)

Fig. 4. Partitioning scheme along the longitudinal axis of each rib. The 10 colors depict the 20 different cylindrical segments, 10 within each rib. (For interpretation of the references to color in this figure legend, the reader is referred to the web version of this article.)
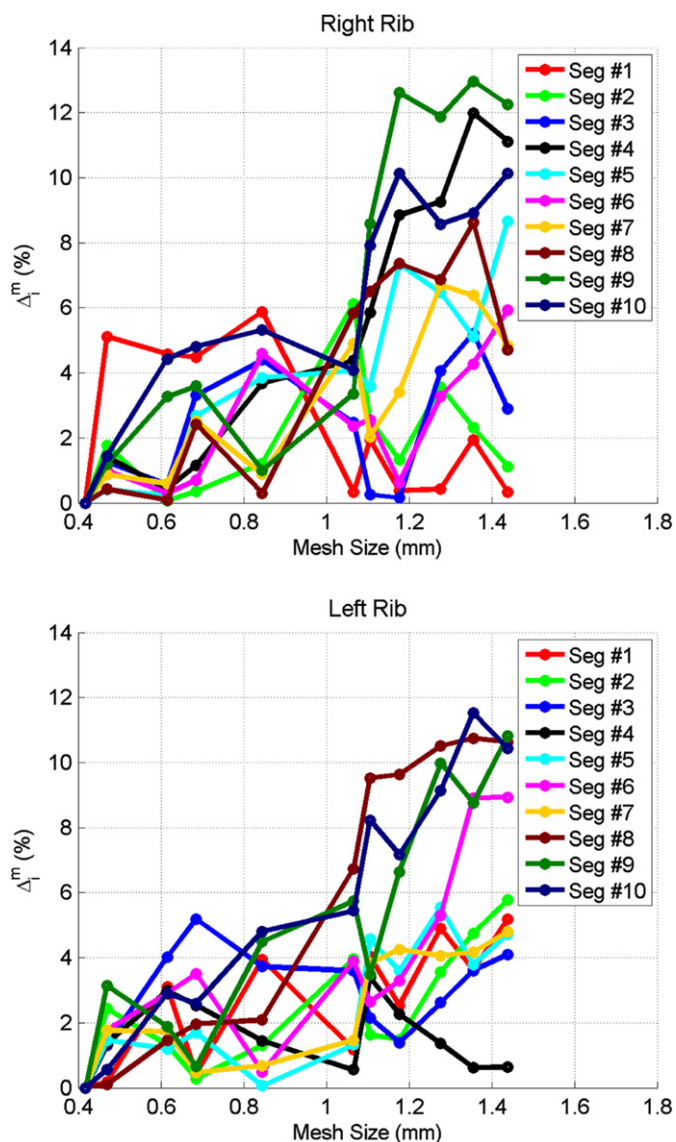
Fig. 5. Percent change in von Mises stress within right and left rib segments relative to the densest mesh model, as a function of average element edge length. Following is the 11 different average element edge lengths used: 0.416 mm, 0.468 mm, 0.618 mm, 0.684 mm, 0.844 mm, 1.065 mm, 1.105 mm, 1.176 mm, 1.276 mm, 1.354 mm, and 1.438 mm. There is a dramatic increase in Δ_i^m after $m = 1.065$ mm. (For interpretation of the references to color in this figure legend, the reader is referred to the web version of this article.)

ribs (Fig. 6). There is an associated increase in stress along the anterolateral aspects of the ribs (Segments 2–4). As per design of the boundary condition, the posterior rib tubercles pivoted on the transverse process cartilage apophyses, resembling a lever pivoting on a fulcrum, in keeping with the hypothesis proposed in the literature for posterior rib fractures in child abuse (Kleinman and Schlesinger, 1997; Worn and Jones, 2007). As expected, there is an associated increase in stress along the rib tubercles (Segment 10). These two areas of increased stress along the ribs correlate with the locations of commonly seen infant rib fractures (Kleinman et al., 1996).

3.2.2. Variations in bone material properties

When Young's modulus was varied between low and high values, the average stress (Fig. 7) along the body of both ribs (Segments 1–7) was affected more than the remaining portions of
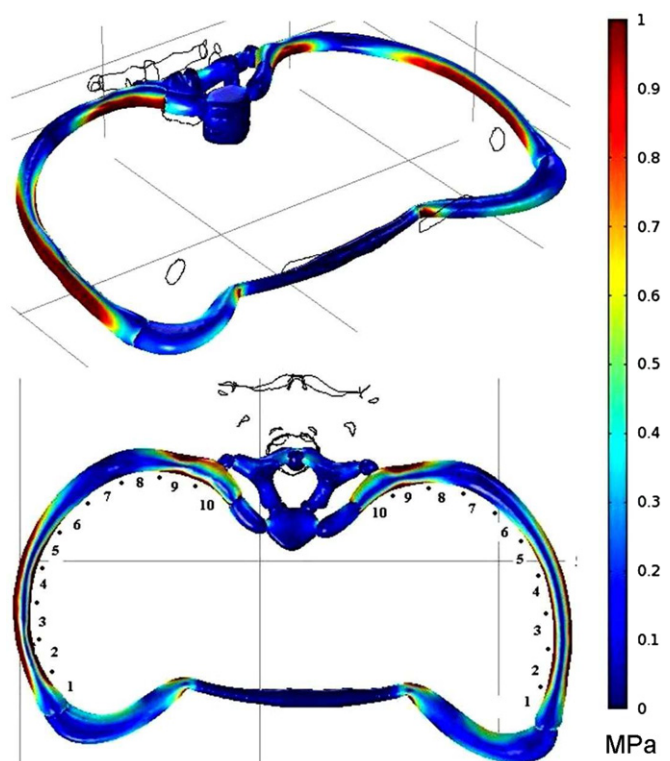
Fig. 6. Two views of the simulation results using baseline values for the material properties and anterior–posterior chest compression depth. Hotter colors indicate areas of increased von Mises stress, while cooler colors indicate areas of decreased stress. Numbers 1–10 along the ribs' inner longitudinal contours within the lower figure correspond to the aforementioned partitioning scheme. (For interpretation of the references to color in this figure legend, the reader is referred to the web version of this article.)

the ribs (Segments 8–10). These simulation results were similar between the right and left ribs, with slight differences likely due to the inherent anatomic right–left asymmetry.

Varying Poisson's ratio between the low and high values had no effect on the average stress along both ribs (Fig. 8). The distribution of stress between the right and left ribs was very similar with only slight differences in magnitude due to the asymmetry of the model.

3.2.3. Variations in cartilage material properties

The low value of Young's modulus resulted in the anterior costal cartilage absorbing all of the anteriorly applied displacement and offered no resistance to the applied posterior displacement. As a result, the average stress within all rib segments was extremely low (Fig. 9). The percent change in the average stress using the low Young's modulus approached −100%, suggesting that there was almost no stress along the ribs. With the high value of Young's modulus, the change in average stress along the posterior rib arcs (Segments 8 and 9) was greater than the remaining anterolateral ribs bodies (Segments 1–6). The stress percent change using the high Young's modulus shows a significant increase in stress over the baseline value, with a disproportionate increase in stress along the posterior rib arcs (Segments 8 and 9). There were slight differences in the magnitude of stress between the right and left ribs due to anatomical asymmetry.

The average stress along both ribs changed only slightly with variations in Poisson's ratio (Fig. 10), and was never more than 5.3% different (Segment 1), with most around 1%. This is within the range of error that may have been generated from the FE meshing and analysis. There were only minor differences in stress
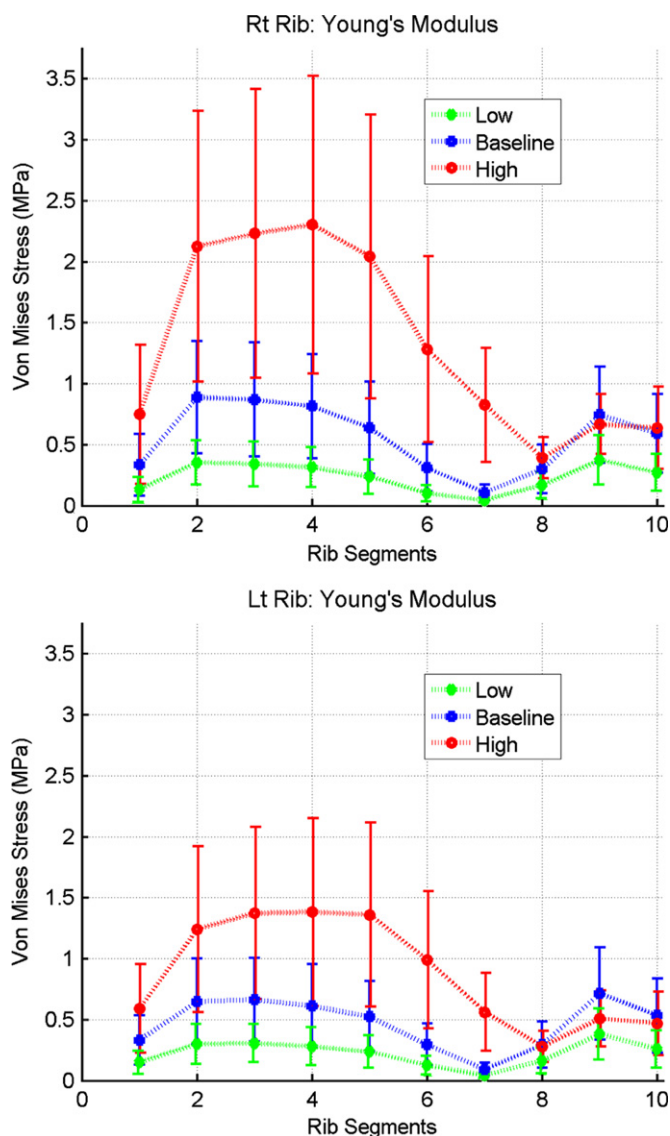
Fig. 7. Longitudinal stress profile along the right and left sixth ribs, with varying bone's Young's modulus. Average ± standard deviation of the von Mises stresses within each rib segment are shown.

Fig. 8. Longitudinal stress profile along the right and left sixth ribs, with varying bone's Poisson's ratio. Average ± standard deviation of the von Mises stresses within each rib segment are shown.

magnitude between the right and left ribs due to the anatomical asymmetry.

3.2.4. Variations in chest compression

Varying the degree of anterior–posterior compression only altered the magnitude of the stress response along the rib, and not the distribution of the stress response (Fig. 11).

4. Discussion

To build a foundation for investigating infant rib fracture, we developed an anatomically detailed FE model, and performed a sensitivity analysis to evaluate the effects of bone and cartilage material properties on stress during an abusive type of chest compression. We found that Young's modulus for both bone and cartilage had a significant effect on magnitude and distribution of stress in the bone, but variations in Poisson's ratio for either material had no effect. This might be expected given the material model selected. A sensitivity analysis in adult rib (Li et al., 2010a, 2010b) investigated parameters of an elastic–plastic model for
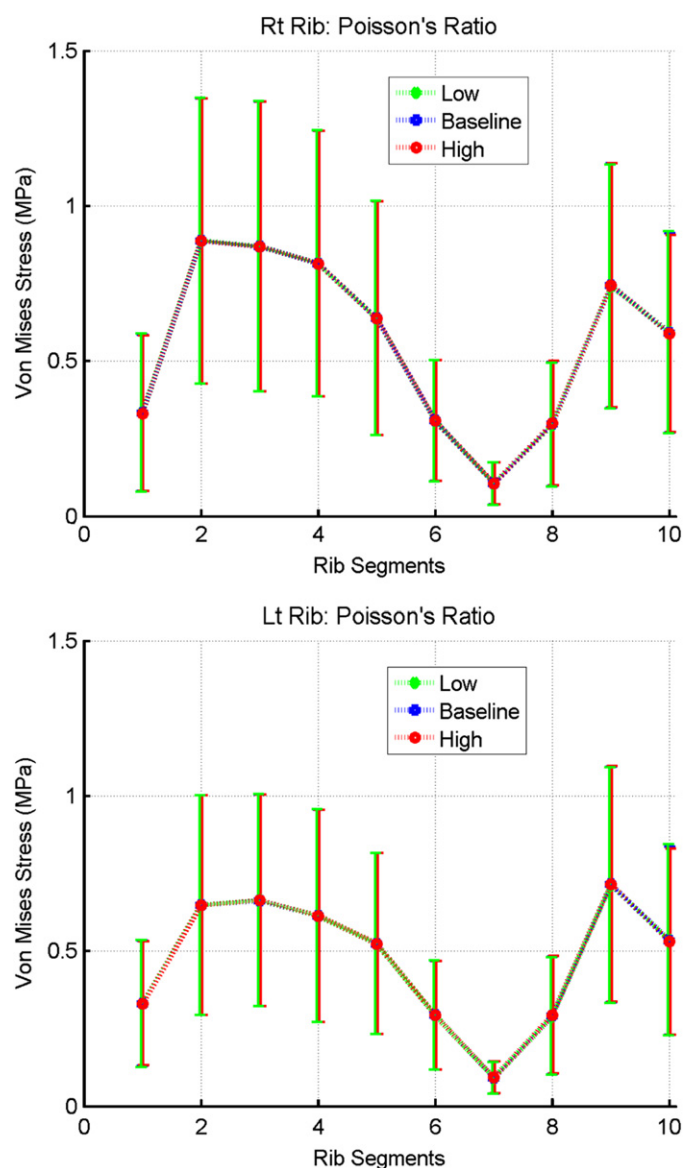
cortical and trabecular bone. Similar to our study, they report a significant effect of Young's modulus on the magnitude of stress. The plastic parameters for their model (yield stress and tangential modulus) significantly affected the stress in cortical bone, but produced negligible affects in the trabecular bone. The pediatric rib bone material property studies available in the literature do not provide stress–strain graphs for infant rib, and it is difficult to identify an appropriate constitutive model for this young age. It is likely that the pediatric rib bone exhibits both elastic and plastic behavior, but the material properties to define these behaviors are unknown. Additional data regarding the stress–strain response of infant rib bone are required before these constitutive models can be used in the FE analysis. Similarly, adult cartilage is typically characterized as viscoelastic and hyperelastic (Brown et al., 2009; Lu and Mow, 2008; Natali and Meroi, 1990), and the use of a linear elastic model in this study is likely a simplification of the real material. Despite this limitation, the sensitivity analysis found cartilage properties significantly affect the stress in the rib, supporting the need to get accurate material properties in
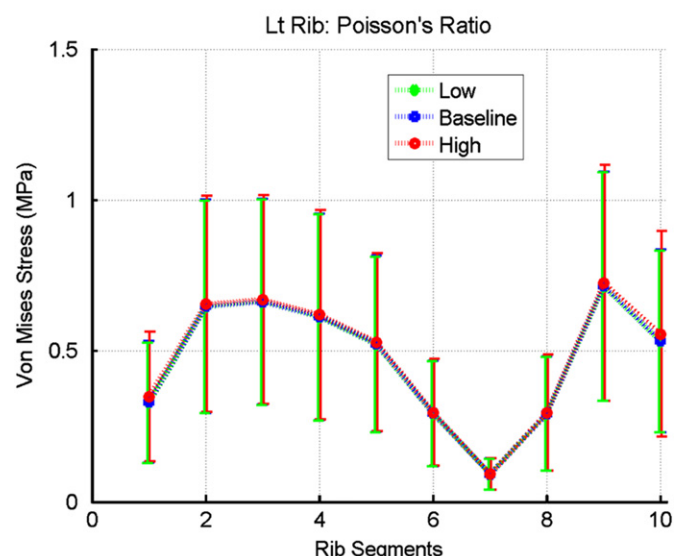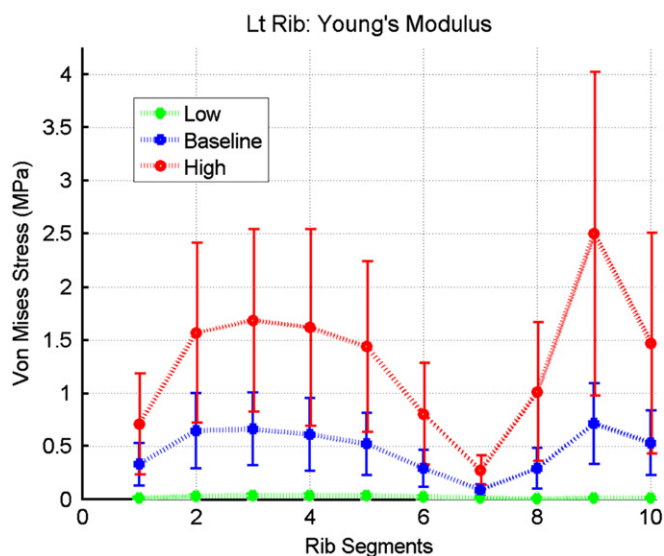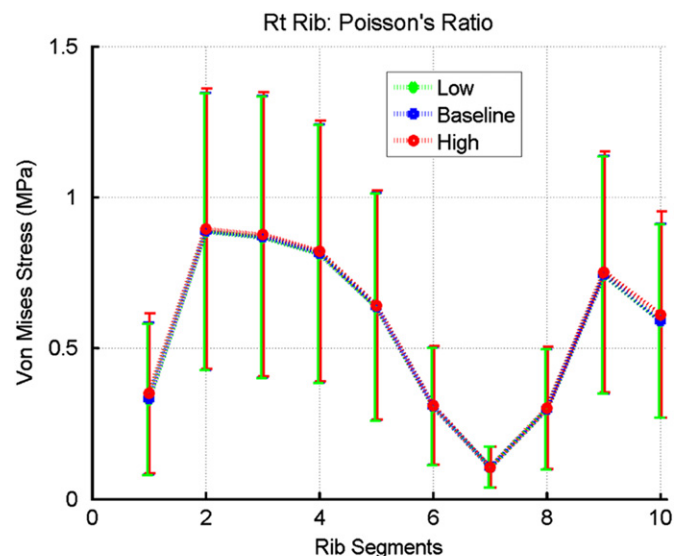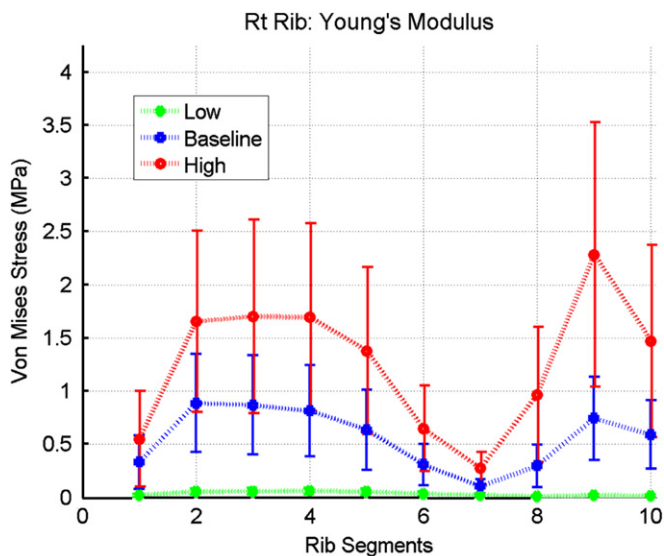
Fig. 9. Longitudinal stress profile along the right and left sixth ribs, with varying cartilage's Young's modulus. Average ± standard deviation of the von Mises stresses within each rib segment are shown.

Fig. 10. Longitudinal stress profile along the right and left sixth ribs, with varying cartilage's Poisson's ratio. Average ± standard deviation of the von Mises stresses within each rib segment are shown.

both bone and cartilage before predictions of infant rib fracture can be made.

With very limited data on infant cortical bone, no published data on infant trabecular bone, and not being able to separate cortex from trabeculae on CT, the homogeneous solid ribs were assigned Young's moduli of cortical bone. The low and baseline assignments may be over-estimations as the softer trabecular core was not taken into account. However, the percentage of trabecular core within the rib increases with increasing age. In males, the representative ratios of trabeculae to total rib cross-sectional area with age are as follows: 37% in 0–4 year-olds, 51% in 10–14 year-olds, 65% in 30–34 year-olds, and 73% in > 70 year-olds (Takahashi and Frost, 1966). This suggests that the contribution of trabecular bone in infants is much smaller than in adults, and the low and baseline moduli may only be slight over-estimations. Despite the potential for over-estimation, we still found the modulus of bone to significantly affect the stress distribution during chest compression. This finding would be the same at lower moduli.

The applied force while gripping a child is unknown. There-fore, we used CPR compression regulations as a baseline and

selected a wide range of displacements for the parametric analysis. As expected, changing compression displacement did not alter the distribution of stress, but linearly affected the maximum stress in the rib. It is unknown what stress causes fracture in the infant rib. Fracture threshold data and forces applied during child abuse must be identified before predictions of rib fracture can be made with the FE analysis.

A natural extension of this work is to expand upon the single rib pair model to include multiple contiguous rib pairs, associated vertebral bodies, and subjacent soft tissue structures, in identifying their contributions. In addition, given the findings in our study, the primary importance will be on obtaining age-appro-priate material properties of cortical and trabecular rib bone and cartilage, and examining the level and effect of perichondrium in infants of this age. New high resolution CT images may provide better delineation between cortical and trabecular bone, thus enabling more accurate modeling of the rib.

One of the strengths in this study was the detailed anatomical geometry extracted from CT scans of an infant. This resulted in a natural asymmetry between the two sides of the ribs in the model. This asymmetry altered the magnitude of the stress
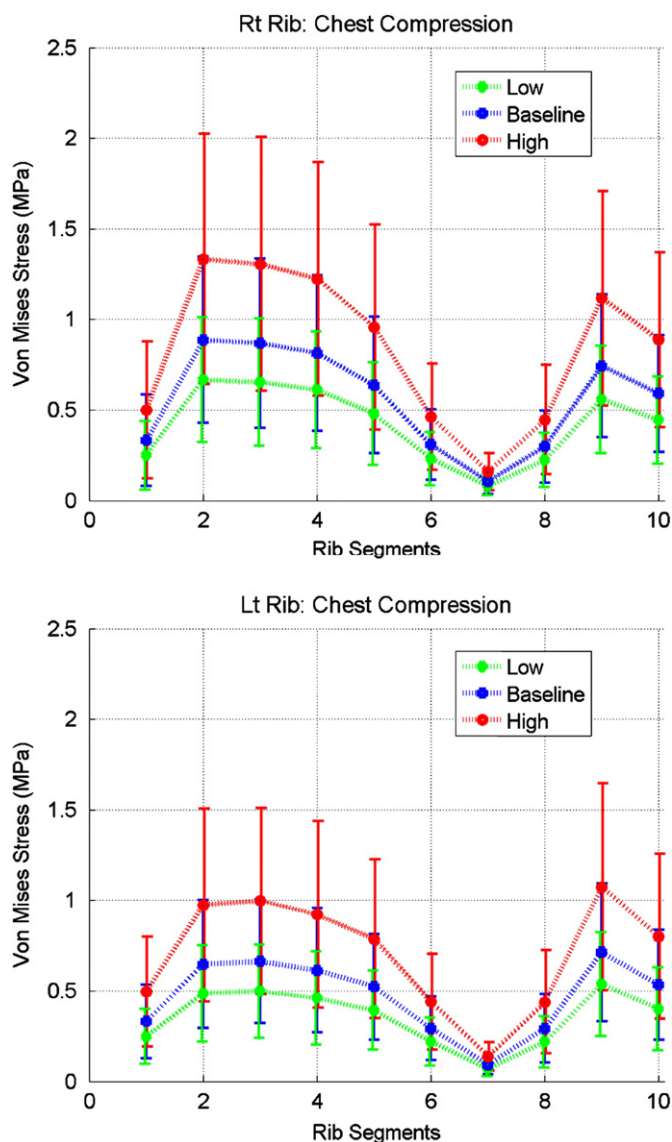
Fig. 11. Longitudinal stress profile along the right and left sixth ribs, with varying chest compression depth. Average $\pm$ standard deviation of the von Mises stresses within each rib segment are shown.

following chest compression. If rib asymmetry is typical in most infants, then this suggests that one side of an infant's ribs may be more susceptible to rib fracture than the other. In addition, it is likely that perpetrators of abuse display a handedness when gripping a child, and the force applied to one of the ribs will be slightly greater than the force applied to the other. Therefore, predictions of fracture in infant ribs from abuse will rely on the handedness of the abuser and the asymmetry in the infant ribs. This relationship merits further investigation as it could be used forensically to help identify perpetrators of abuse.

The sensitivity analysis of this study found that predictions of infant rib fracture from child abuse will depend heavily on the (1) elastic modulus of rib bone and cartilage with developmental age, (2) asymmetry in the infant's ribs, and (3) force applied by the perpetrator while gripping the child. Currently, very little data is available on these features. The FE analysis is a valuable tool that can potentially be used to understand mechanisms of rib fracture in infants, but predictions of fracture from child abuse using the FE modeling will be hindered until the above factors have been experimentally determined.

Conflict of interest statement

Acknowledgments

References

Abé, H., Hyayashi, K., Sato, M., 1996. Data Book on Mechanical Properties of Living Cells Tissues and Organs. Springer-Verlag, New York.

American Heart Association, 2006. 2005 American Heart Association guidelines for cardiopulmonary resuscitation and emergency cardiovascular care of pediatric and neonatal patients: neonatal resuscitation guidelines. Pediatrics 117, e1029–e1038.

Betz, P., Liebhardt, E., 1994. Rib fractures in children—resuscitation or child abuse? International Journal of Legal Medicine 106, 216–218.

Boal, D.K., 2008. Child abuse. In: Slovis, T.L. (Ed.), Caffey's Pediatric Diagnostic Imaging, 11th edition Mosby Elsevier, Philadelphia, pp. 2816–2830.

Brown, C.P., Nguyen, T.C., Moody, H.R., Crawford, R.W., Oloyeda, A., 2009. Assessment of common hyperelastic constitutive equations for describing normal and osteoarthritic articular cartilage. Proceedings of the Institution of Mechanical Engineers, Part H 223, 643–652.

Charpail, E., Trosseille, X.l., Petit, P., Laporte, S., Lavaste, F., Vallancien, G., 2005. Characterization of PMHS ribs: a new test methodology. Stapp Car Crash Journal 49, 183–198.

Donelson, S.M., Gordon, C.C., 1996. 1995 Matched Anthropometric Database of US Marine Corps Personnel: Summary Statistics.

Forman, J.L., del Pozo de Dios, E., Kent, R.W., 2010. A pseudo-elastic effective material property representation of the costal cartilage for use in finite element models of the whole human body. Traffic Injury Prevention 11, 613–622.

Forman, J.L., Kent, R.W., 2011. Modeling costal cartilage using local material properties with consideration for gross heterogeneities. Journal of Biomechanics 44, 910–916.

Gray, H., 1974. Anatomy, Description and Surgical. Running Press, Philadelphia, PA.

Greer, A., 2006. Numerical Modeling for the Prediction of Primary Blast Injury to the Lung. Master's Thesis, University of Waterloo.

Ito, O., Ohhashi, K., Dokko, Y., 2009. Development of Adult and Elderly FE Thorax Skeletal Models. Society of Automotive Engineers 2009-09B-0107.

Kemper, A., McNally, C., Pullins, C.A., Freeman, L.J., Duma, S.M., 2005. The biomechanics of human ribs: material and structural properties from dynamic tension and bending tests. Stapp Car Crash Journal 51, 235–273.

Kleinman, P.K., 1990. Diagnostic imaging in infant abuse. American Journal of Radiology 155, 703–712.

Kleinman, P.K., Marks, S.C., Nimkin, K., Rayder, S.M., Kessler, S.C., 1996. Rib fractures in 31 abused infants: postmortem radiologic–histopathologic study. Radiology 200, 807–810.

Kleinman, P.K., Nimkin, K., Belanger, P., 2000. Distribution of rib fractures in suspected child abuse: a ten year study using high detail skeletal surveys. In: European Society of Paediatric Radiology 37th Annual Congress, Lisbon, Portugal.

Kleinman, P.K., Schlesinger, A.E., 1997. Mechanical factors associated with posterior rib fractures: laboratory and case studies. Pediatric Radiology 27, 87–91.

Lau, A., Oyen, M.L., Kent, R.W., Murakami, D., Torigaki, T., 2008. Indentation stiffness of aging human costal cartilage. Acta Biomaterialia 4, 97–103.

Li, Z., Kindig, M.W., Subit, D., Kent, R.W., 2010a. Influence of mesh density, cortical thickness and material properties on human rib fracture prediction. Medical Engineering and Physics 32, 998–1008.

Li, Z., Kindig, M.W., Kerrigan, J.R., Untaroiu, C.D., Subit, D., Crandall, J.R., Kent, R.W., 2010b. Rib fractures under anterior–posterior dynamic loads: experimental and finite-element study. Journal of Biomechanics 43, 228–234.

Lonergan, G.J., Baker, A.M., Morey, M.K., Boos, S.C., 2003. From the archives of the AFIP. Child abuse: radiologic–pathologic correlation. Radiographics 4, 811–845.

Lu, X.L., Mow, V.C., 2008. Biomechanics of articular cartilage and determination of material properties. Medicine and Science in Sports and Exercise 40, 193–199.

Mahmoodian, R., Leasure, J., Gadikota, H., Capaldi, F., Siegler, S., 2009. Mechanical properties of human fetal talus. Clinical Orthopedic Related Research 467, 1186–1195.

Mizuno, K., Iwata, K., Deguchi, T., Ikami, T., Kubota, M., 2005. Development of a three-year-old child FE model. Traffic Injury Prevention 6, 361–371.

Natali, A., Meroi, E., 1990. Nonlinear analysis of intervertebral disk under dynamic load. Journal of Biomechanical Engineering 112, 358–363.

Netter, F., 2003. Atlas of Human Anatomy. Icon Learning Systems, Teterboro, NJ.

Niu, Y., Shen, W., Stuhmiller, J.H., 2007. Finite element models of rib as an inhomogeneous beam structure under high-speed impacts. Medical Engineering and Physics 29, 788–798.

Openshaw, P., Edwards, S., Helms, P., 1984. Changes in rib cage geometry during childhood. Thorax 39, 624–627.

Pfefferle, K.L., Litsky, A., Donnelly, B., Bolte, IV J., 2007. Biomechanical properties of the excised pediatric human rib. In: Injury Biomechanics Research: Proceedings of the Thirty-fifth International Workshop.

Reece, R.M., 1993. Child Abuse: Medical Diagnosis and Management. Lea & Febiger, Philadelphia.

Reece, R.M., 2002. What the literature tells us about rib fractures in infancy. In: National Conference on Shaken Baby Syndrome, SBS Quarterly, Fall.

Ruan, J., El-Jawahri, R., Chai, L., Barbat, S., Prasad, P., 2003. Prediction and analysis of human thoracic impact responses and injuries in cadaver impacts using a full human body finite element model. Stapp Car Crash Journal 47, 299–321.

Takahashi, H., Frost, H.M., 1966. Age and sex related changes in the amount of cortex of normal human ribs. Acta Orthopaedica Scandinavica 37, 122–130.

Trickey, W.R., Baaijens, F.P.T., Laursen, T.A., Alexopoulos, L.G., Guilak, F., 2006. Determination of the Poisson's ratio of the cell: recovery properties of chondrocytes after release from complete micropipette aspiration. Journal of Biomechanics 39, 78–87.

Vaziri, A., Nayeb-Hashemi, H., Akhavan-Tafti, B., 2009. Computational model of rib movement and its application in studying the effects of age-related thoracic cage calcification on respiratory system. Computer Methods in Biomechanical Engineering, 1–8.

Viano, D.C., 1986. Biomechanics of bone and tissue: a review of material properties and failure characteristics. In: Proceedings–Society of Automotive Engineers, 33–63.

Wagner, C.H., 1988. The pianist's hand: anthropometry and biomechanics. Ergonomics 31, 97–131.

Worn, M.J., Jones, M.D., 2007. Rib fractures in infancy: establishing the mechanisms of cause from the injuries—a literature review. Medical Science and the Law 47, 200–212.

Yamada, H., 1970. In: Evans, F.G. (Ed.), Strength of Biological Materials. Williams and Wilkins, Baltimore, MD.

Yoganandan, N., Pintar, F.A., 1998. Biomechanics of human thoracic ribs. Journal of Biomechanical Engineering 120, 100–104.